Dynamical and Thermodynamical Drivers of Humidity Variability in the Tropical Western Pacific

Adrian Mark Tompkins[1], Alejandro Casallas[1,2], Michie Vianca De Vera[3]

[1] Earth System Physics, Abdus Salam International Centre for Theoretical Physics, Trieste, 34151, Italy

[2] Department of Mathematics and Geoscience, University of Trieste, Trieste, 34127, Italy

[3] Department of Climate, Meteorology, and Atmospheric Sciences, University of Illinois Urbana-Champaign, Illinois, 61801, USA

Contents of this file

Introduction

In Figures S1 and S2, we depict the contribution of sea surface temperature (SST), humidity, temperature, and clouds on the top-of-the-atmosphere (TOA) outgoing longwave (LW) radiation for clear sky and all-sky conditions, respectively. It is derived by selecting 90 example days in reversal events, and 90 during clustered conditions, and then using the 1D RRTMG column model offline on each region and each day we swap out the fields of temperature, humidity, SST, and clouds in turn using alternative day in a n opposite organized/reversal periods selected at random. The calculation underscores the essential role of humidity in regulating LW clear-sky radiation, as moisture significantly impacts atmospheric opacity, while cloud properties emerge as the primary driver for variability in all sky radiation, likely attributable to cloud fraction.

Figures S3 and S4 show the diabatic feedbacks observed during the MAM (Figure S3) and JJA (Figure S4) seasons of 2017. In MAM, all diabatic feedbacks predominantly support clustering, barring the latent heat (LH) feedback, which is mitigated by wind enhancement outside convective zones, and the shortwave (SW) clear sky feedback, influenced by anvils, mirroring findings from idealized studies. Notably, during reversal events in MAM, the LW clear-sky feedback also opposes clustering by favoring warmest SST regions associated with clear skies, inducing warming and a negative feedback. Conversely, during the JJA season, all diabatic feedbacks contribute to clustered convection, although their influence alone isn't potent enough to enforce clustering. This observation aligns with the SST-TCWV (total column water vapor) relationship, indicating that convection tends to maintain a random configuration despite these feedbacks.

Figure S5 assesses the impact of stability, moisture, and wind speed on the LH flux feedback, employing a machine learning approach outlined in the method section. Our results demonstrate that when convection is clustered, the feedback is negative, whereas in a uniformly random configuration, the feedback aligns positively, mirroring idealized studies. Interestingly, our study diverges from idealized findings, wherein moisture structures and stability typically dominate. Instead, we observe that in our study regions, regardless of convective states, wind speed emerges as the most influential contributor to the LH flux feedback.

Figures S6 and S7 provide lead-lag composites of two of our examined regions for boreal winter/spring, akin to Figure 9 in the main text. In Figure S6, focusing on the area spanning 147-157E, we observe an equatorial Rossby wave-like pattern characterized by a symmetric outgoing

LW anomaly relative to the equatorial region. Turning to Figure S7, which represents the region between 156-166E, we witness the evolution of a similar equatorial Rossby wave-like pattern. This pattern traverses the region and subsequently engenders an outgoing LW symmetric anomaly concerning the equator. These findings corroborate the insights outlined in the main text, where we emphasize the significance of wave dynamics in governing the states of convection throughout the boreal winter and spring seasons.

To complement our analysis, we conducted a multivariate rotational empirical orthogonal function (REOF) analysis with SST and TCWV for the primary target region (135-145E). Figure S8 illustrates the combined representation of the first three principal components (PCs) of the REOF results, alongside the SST-TCWV regression. A high degree of similarity is observed between the sum of these PCs and the wave pattern obtained using instead the SST-TCWV regression index, particularly evident during the boreal winter/spring period (R=0.87). Utilizing the sum of the PCs, we constructed a lead-lag composite of 36 events, akin to the depiction in Figure 9 of the main text, focusing on the primary region for the boreal winter/spring season (Figure S9). The results further reinforce the conclusions drawn in the main text, showcasing an equatorial Rossby wave-like pattern. This consistency underscores the robustness and reliability of our findings.

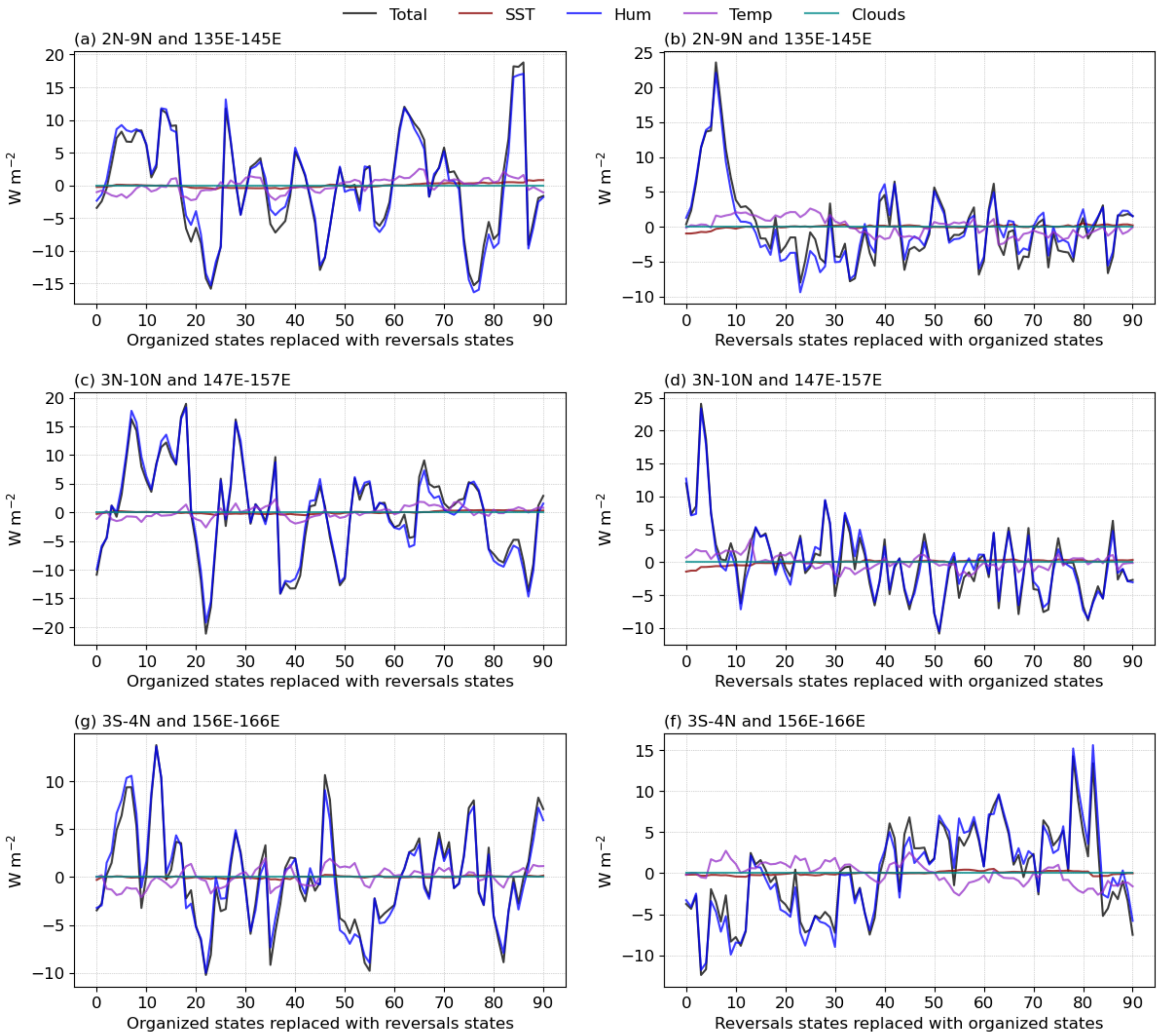

Figure S1. Contributions to clear-sky TOA OLR from SST, specific humidity (Hum), temperature, and cloud components (liquid water, ice, and cloud fraction) for (a-c-e) organized days replaced with reversal events and for (b-d-f) reversal days replaced with organized events. The depicted regions are (a-b) 2N-9N and 135E-145E, (c-d) 3N-10 and 147E-157E, and (e-f) 3S-4N and 156E-166E. The x-axis represents the days on which the replacement was performed.

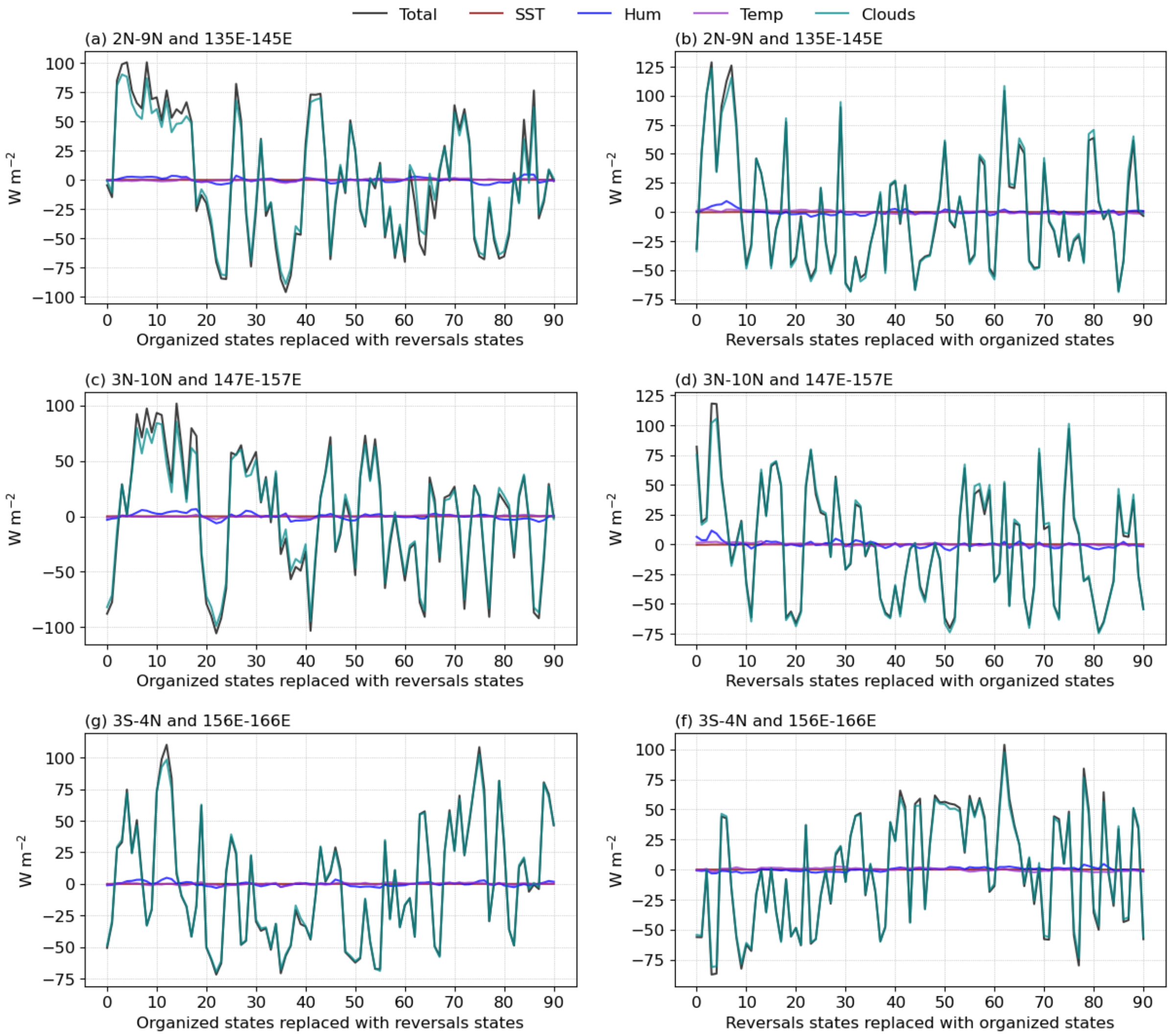

Figure S2. Contributions to all-sky TOA OLR from SST, specific humidity (Hum), temperature, and cloud components (liquid water, ice, and cloud fraction) for (a-c-e) organized days replaced with reversal events and for (b-d-f) reversal days replaced with organized events. The depicted regions are (a-b) 2N-9N and 135E-145E, (c-d) 3N-10 and 147E-157E, and (e-f) 3S-4N and 156E-166E. The x-axis represents the days on which the replacement was performed.

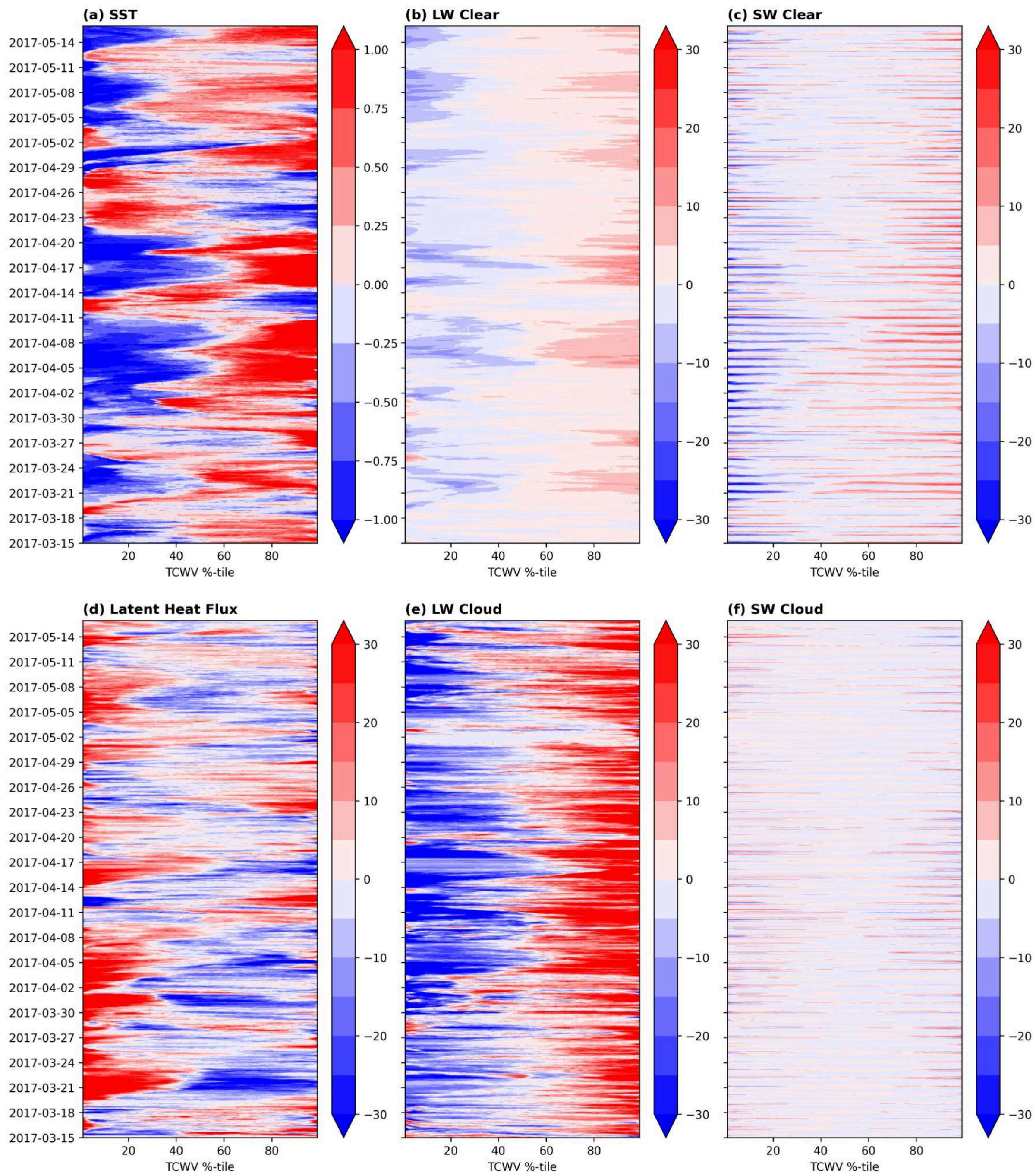

Figure S3. Hovmöller diagram of atmospheric convergence spatial anomaly (positive is warming anomaly of atmosphere) for the boreal winter/spring seasons. (a) SST, (d) surface latent heat, and net atmospheric convergence of (b) LW clear sky flux, (e) LW cloud forcing (total flux - clear), (c) SW clear, and (f) SW cloud fluxes.

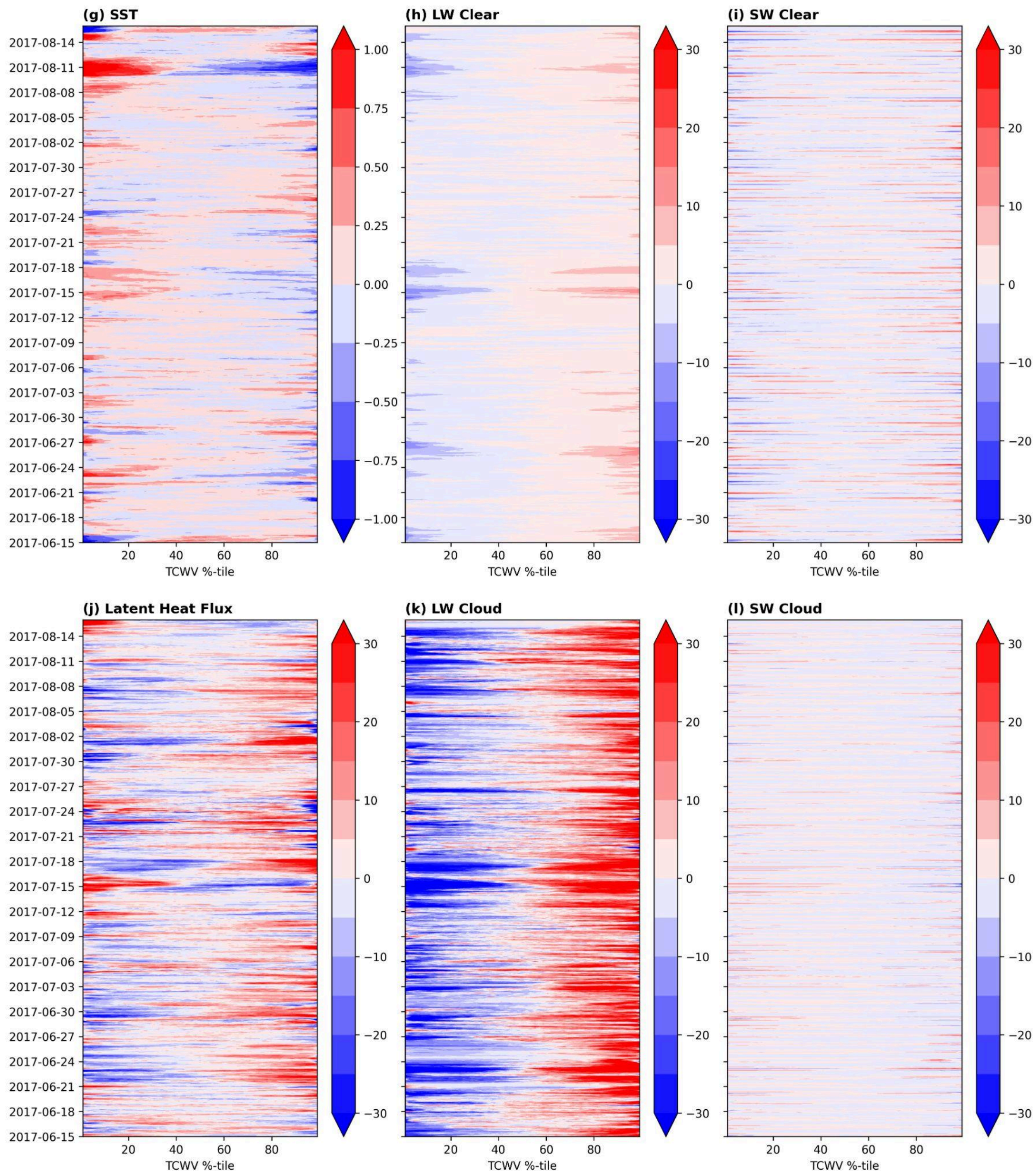

Figure S4. Hovmöller diagram of atmospheric convergence spatial anomaly (positive is warming anomaly of atmosphere) for the boreal summer/autumn seasons. (a) SST, (d) surface latent heat, and net atmospheric convergence of (b) LW clear sky flux, (e) LW cloud forcing (total flux - clear), (c) SW clear, and (f) SW cloud fluxes.

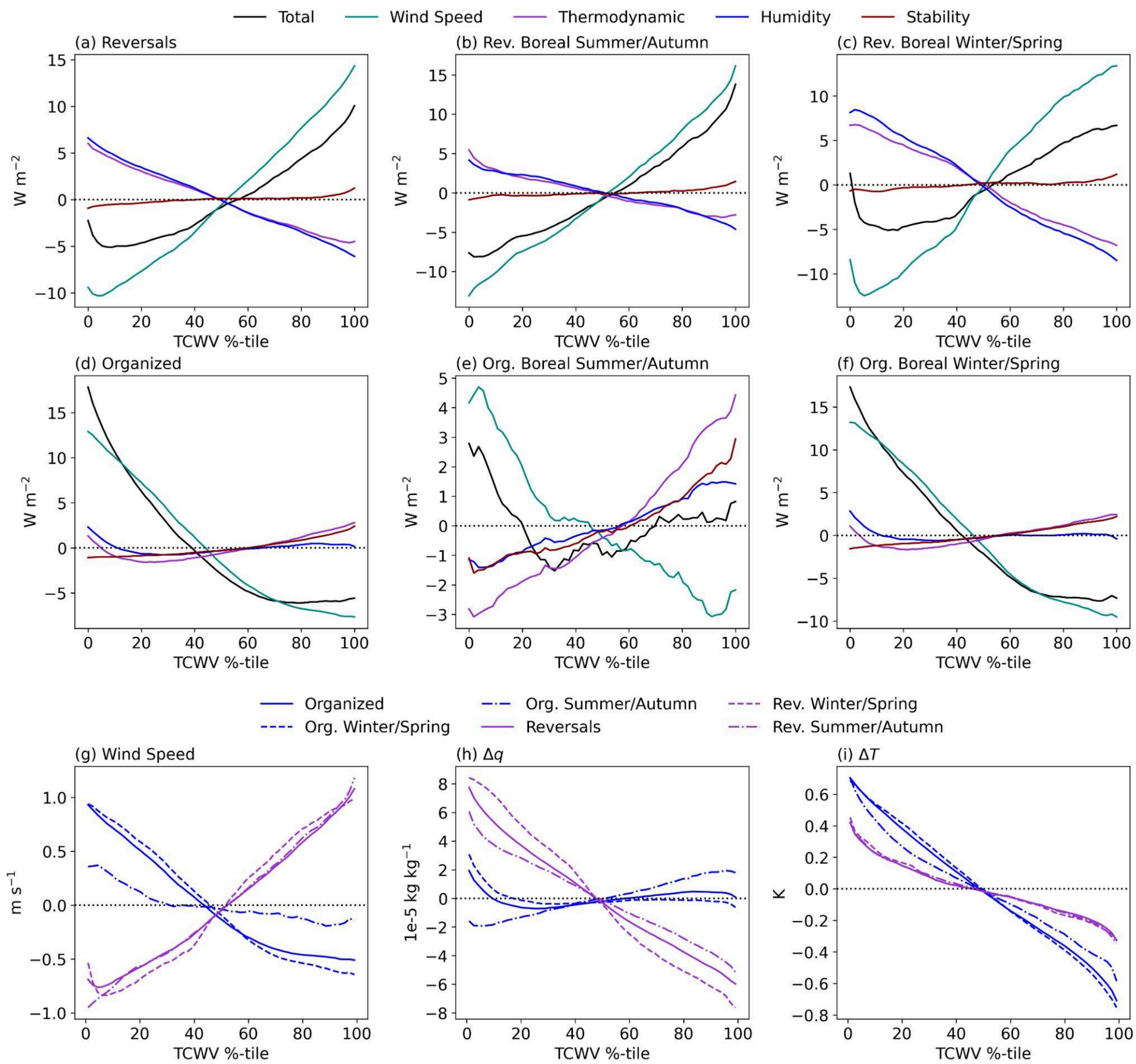

Figure S5. Contributions to LH surface flux perturbations in the reversal regime are depicted for (a) the entire dataset, and separately for (b) boreal summer-autumn and (c) winter-spring. Similarly, contributions are illustrated for the organized regime, encompassing (c) the entire dataset, and for boreal (b) summer-autumn and (c) winter-spring. These contributions emanate from (g) wind speed perturbations, (h) humidity (Δq), and (i) stability (ΔT) differences. Thermodynamic perturbations refer to the combined contribution of ΔT and Δq terms. The calculations are executed using a random forest (RF) algorithm fitted to the ERA5 dataset.

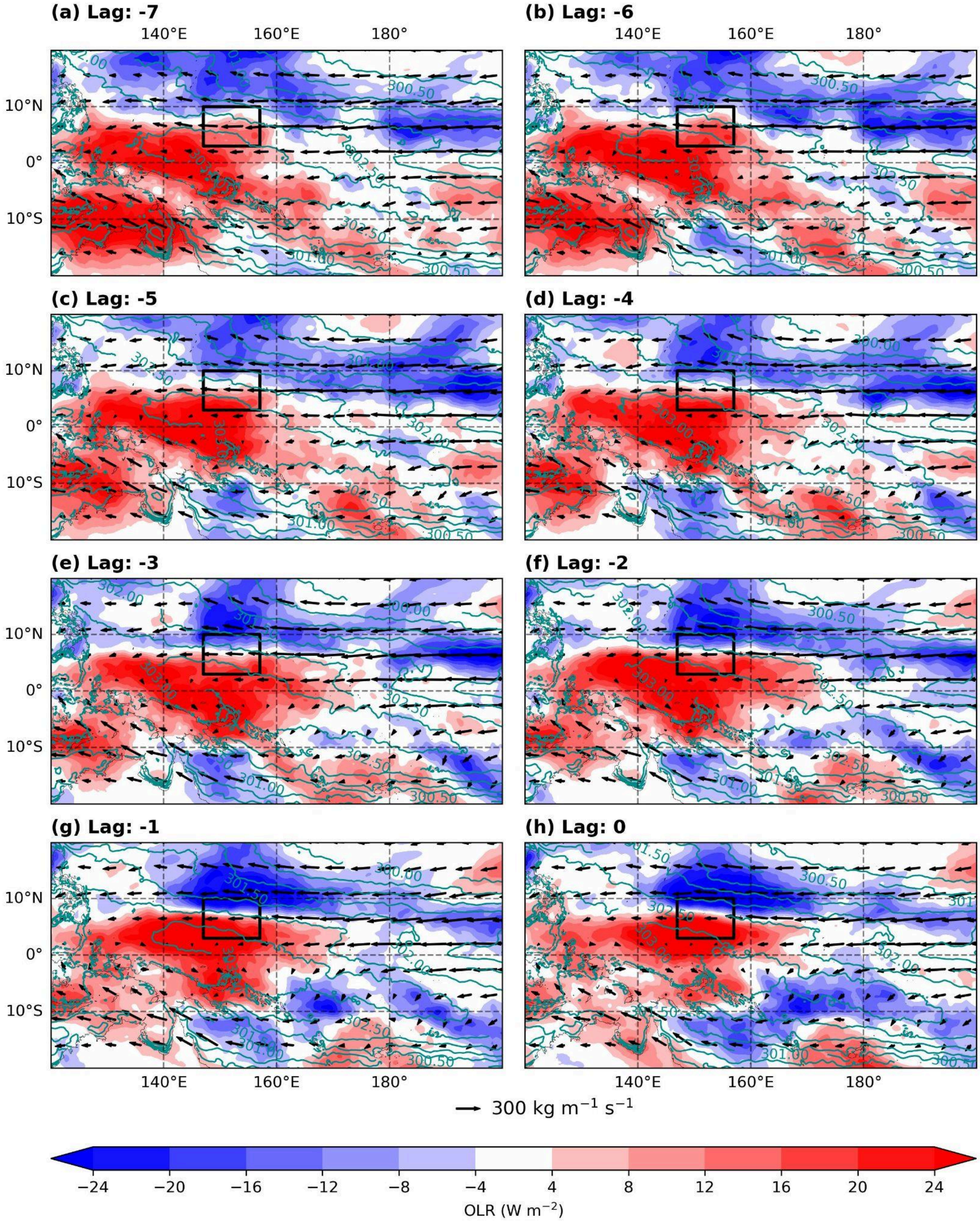

Figure S6. Composite of 46 reversal states on boreal winter-spring months and their related lags. The colors represent the OLR anomaly for each of the lags. The contours are the SST and the arrow's size represents the column integrated water vapor flux (WVF) magnitude and their orientation shows the WVF direction. Notice that each panel indicates the lag in the number of days. The continuous rectangle represents the study area between 3N-10N and 147E-157E.

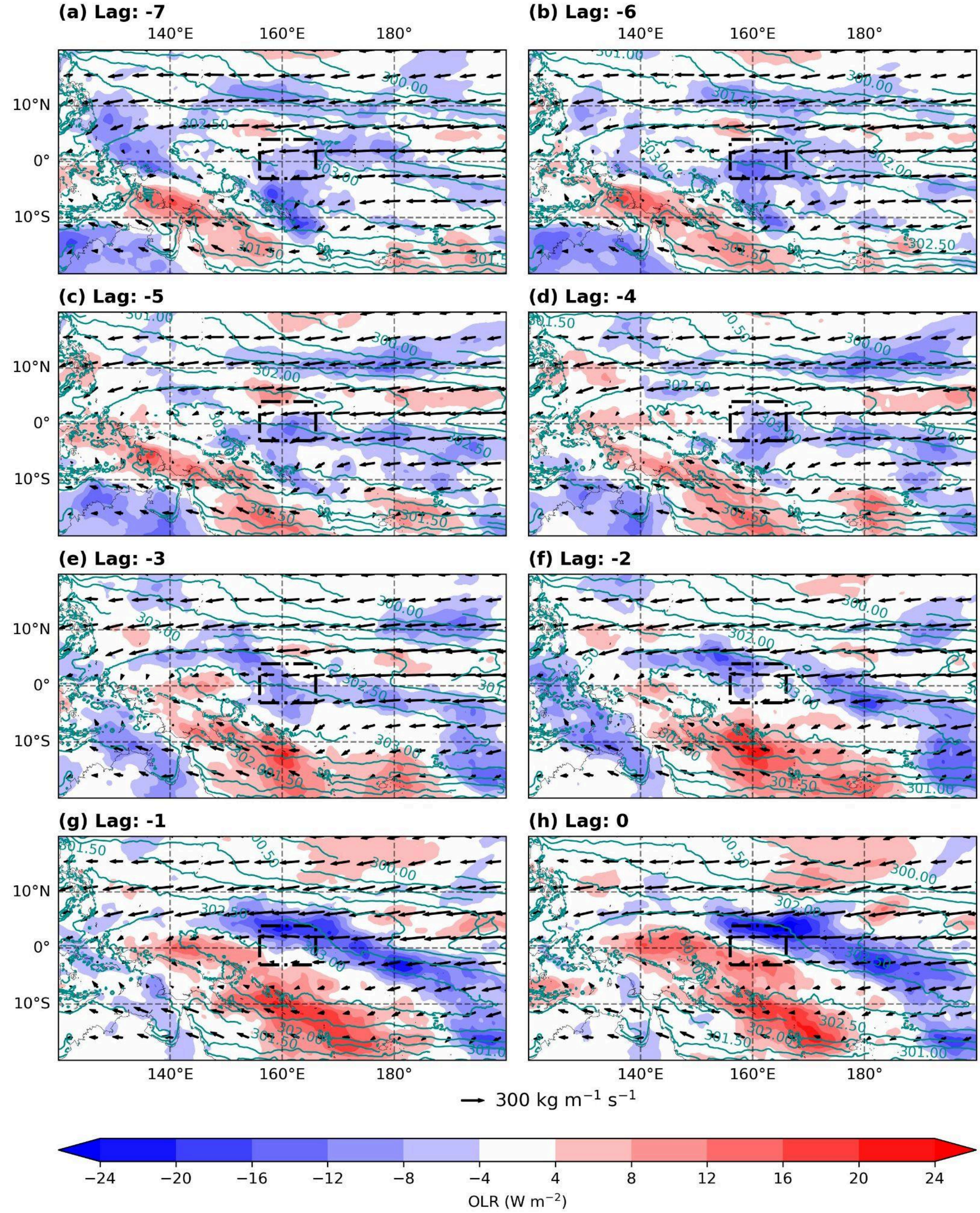

Figure S7. Composite of 41 reversal states on boreal winter-spring months and their related lags. The colors represent the OLR anomaly for each of the lags. The contours are the SST and the arrow's size represents the WVF magnitude and their orientation shows the WVF direction. Notice that each panel indicates the lag in the number of days. The dotted dashed rectangle represents the study area between 3S-4N and 156E-166E.

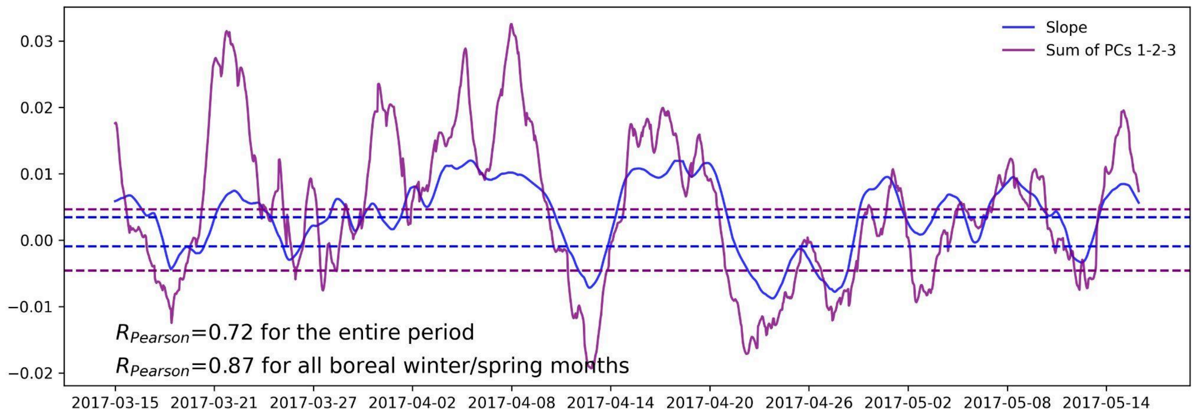

Figure S8. Combined sum of the first three Principal Components (PCs) derived from the multivariate REOF analysis using detrained and deseasonalized data (depicted by the purple line), and the slope ($\frac{dSST}{dTCWVf}$ - represented by the blue line). The horizontal dashed lines indicate values 0.5 standard deviations larger and smaller than the mean for both datasets in the period between 2017-03-15 and 2017-05-15. The Pearson correlation is ≈ 0.87 for all boreal winter/spring months and ≈ 0.72 for the entire study period.

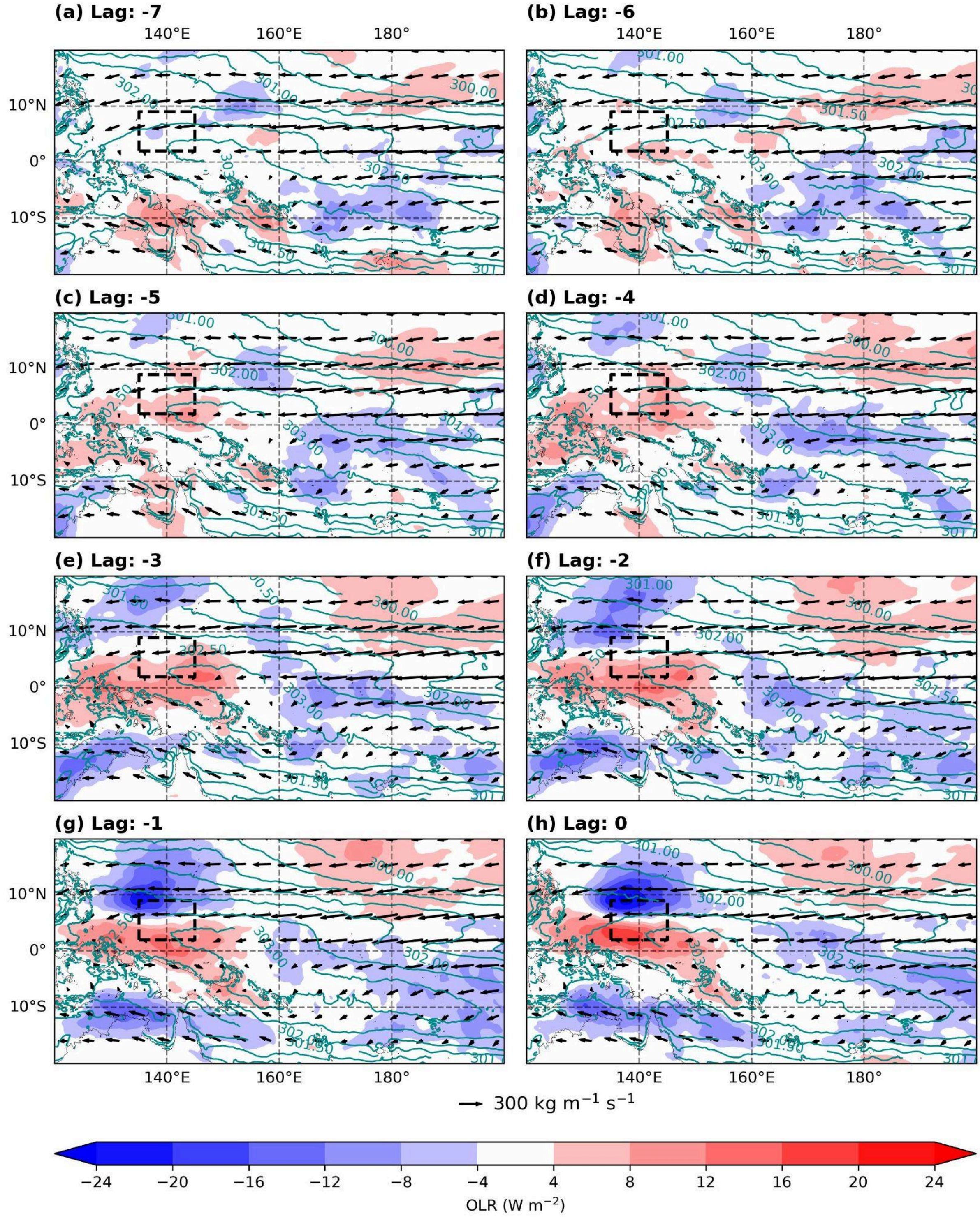

Figure S9. Composite of 37 reversal states on boreal winter-spring months and their related lags calculated using the sum of the first three PCs of the multivariate REOF analysis. The colors represent the OLR anomaly for each of the lags. The contours are the SST and the arrow's size represents the WVF magnitude and their orientation shows the WVF direction. Notice that each panel indicates the lag in the number of days. The dashed rectangle represents the study area between 2N-9N and 135E-145E.